

An integral field spectroscopic study of stellar and ionized gas properties around edge-on disk galaxies in the stellar mass range $9 < \log M_* < 11$

Guinevere Kauffmann^{1*}, Richard D’Souza², Antonela Monachesi³

¹*Max-Planck Institut für Astrophysik, 85748 Garching, Germany*

²*Vatican Observatory, Specola Vaticana, V-00120, Vatican City State*

³*Universidad de La Serena, Avda. Raul Bitran 1305, La Serena, Chile*

21 July 2025

ABSTRACT

We analyze the stellar light, 4000 Å break and emission line profiles of 82 edge-on disk galaxies from the MaNGA survey. We characterize the stellar light profiles perpendicular to the disk plane using two parameters: a) the power law slope of the thick disk component, 2) the transition radius where the profile flattens. The 4000 Å break profiles perpendicular to the plane are characterized by the number of significant changes in slope (breaks) and by the change in $D_n(4000)$ from inner to outer disk. The slope correlates tightly with the stellar mass of the galaxy over the stellar mass range $10^9 < \log M_* < 10^{10} M_\odot$. More massive galaxies have more extended thick disks. The slope and transition radius exhibit large scatter for galaxies more massive than $10^{10} M_\odot$. Half the sample have older stellar populations in their thick disks, a third have flat $D_n(4000)$ profiles and 15% have younger thick disks. The $D_n(4000)$ profiles exhibit as many as 4 separate breaks. There are more breaks in massive galaxies with bulges and more extended thick disks. This may indicate that the breaks are produced by more frequent accretion events in such systems. The extraplanar H α EQW correlates most strongly with the specific star formation rate of the galaxy, and the [OII]/H α ratio increases with distance from the disk plane. This increase is most apparent for massive galaxies with extended thick disk components and low SFR/ M_* . These findings support the hypothesis that the larger [OII]/H α ratios may be caused by ionization from evolved stars.

Key words: galaxies:spiral, galaxies: stellar content, galaxies:structure, galaxies:halos

1 INTRODUCTION

The study of edge-on disk-dominated galaxies provides important information about the 3-dimensional distribution of stars, gas and dark matter in these systems. Early work in the 1980’s (e.g. Van der Kruit & Searle 1981, Van der Kruit 1988) was based on surface photometry from photographic plates that reached limiting surface brightnesses of 22 magnitudes arcsec⁻² in the optical. To model the light profiles, these authors invoked an exponential distribution of stars in the radial direction and adopted an isothermal sheet approximation to describe the structure of the disk in the vertical direction. The radial structure was proposed to be regulated by the angular momentum structure in the proto-galaxy (Freeman 1974; Gunn 1982), while the verti-

cal thickness of the disk was regulated by so-called secular processes, including heating by molecular clouds and spiral arms, and was believed to carry no information about the structure of the proto-galaxy.

The thin disk scale height of nearby disk galaxies is typically less than 1 kpc. The existence of vertically extended disk stellar components emerged into the mainstream from studies of counts of stars as a function of distance from the plane of the Milky Way (Gilmore & Reid 1983). In addition, photometric studies had by then revealed that some nearby edge-on galaxies had thickened disks (Van der Kruit & Searle 1981). Later, deep imaging of edge-on early-type spiral (Wu et al 2002) and lenticular galaxies (Pohlen et al 2004) showed that the thick disk components were distinct from the thin disk.

Dalcanton & Bernstein (2000) carried out deep imaging studies reaching limiting magnitudes of 29 mag arcsec⁻²

* E-mail: gamk@mpa-garching.mpg.de

at optical wavelengths. These authors selected 49 extremely late-type, edge-on disk galaxies from the Flat Galaxy Catalog of Karachentsev et al. (1993). The sample was chosen to have no apparent bulges or optical warps so that the galaxies represent undisturbed “pure disk” systems. The main result of this study was that such thin disks are embedded in a low surface brightness red envelope extending to at least 5 vertical disk scale heights above the galaxy mid-plane, with a radial scale length that appeared to be uncorrelated with that of the embedded thin disk. The color of the red envelope was found to be similar from galaxy to galaxy, even when the thin disk is extremely blue, and was consistent with a relatively old (>6 Gyr) stellar population that was not particularly metal-poor (Dalcanton & Bernstein 2002). These authors argued that the ubiquity of the red stellar envelopes implied that the formation of the thick disk is a nearly universal feature of disk formation and is not necessarily connected to the formation of a bulge. One caveat of this work was that the available K-band photometry was relatively shallow and did not allow for very precise constraints on stellar age or metallicity.

There have also been attempts to study how the importance of the thick disk component depends on the mass or circular velocity of the galaxy, Yoachim & Dalcanton (2006) studied the scale heights of the thin and thick disk components of late type galaxies as a function of circular velocity. The average scale height of the thin disk increased from ~ 300 pc for galaxies with $V_c \sim 50$ km/s to 1 kpc for galaxies with $V_c \sim 200$ km/s, while the scale height of the thick disk increased from 1 to 3 kpc over the same circular velocity range. The ratios of the thick and thin disk scale heights and stellar masses were found to decrease with circular velocity. It should be noted that Comeron et al (2011, 2014) repeated this work using kinematic information to deconvolve the “hot” and the “cold” components of the disk. If the mass of the kinematically hot central component of the galaxy was added to the thick disk, the trend in thin-to-thick disk mass ratio as a function of V_c was nearly absent.

Spectroscopic studies of the vertical structure of edge-on disk galaxies, either using slits oriented along the minor axis of the disks, or using integral field units (IFU) have generally focused on the properties of the ionized extra-planar gas detected in emission. Lehnert & Heckman (1996) carried out a study of 50 IR-selected edge-on starburst galaxies and found that extra-planar emission line gas is a common feature of these systems. The filamentary and shell-like morphology of the gas, the increase in line width along the minor axis of the galaxy, and line ratios indicative of shock ionization pointed to a galactic wind origin for this gas. The strength of the emission lines was also found to correlate with the IR luminosity of the galaxies.

More recently, integral field unit (IFU) spectroscopic surveys of galaxies in the local Universe have allowed the extra-planar gas to be studied in large samples of normal disk galaxies. Ho et al (2016) studied a sample of 40 local main-sequence edge-on disk galaxies observed as part of the SAMI Galaxy Survey, and found that emission line kinematics characteristic of galactic winds were more common in galaxies with high star formation surface densities and in galaxies with spectroscopic signatures of recent starbursts. Jones et al (2016) derived average emission line luminosity profiles from stacked spectra of galaxies from the MaNGA

IFU survey and found the largest differences in emission line profiles and emission line ratios occurred when galaxies were split by stellar mass. In particular, the higher oxygen line to Balmer emission line ratios in the outskirts of massive galaxies were taken as evidence for a change in the ionization source of the lines from massive young stars in HII regions in the inner disk, to ionizing radiation from evolved stars in the outer regions.

Theoretical modelling of the origin of thick disk and halo components of galaxies has advanced dramatically in recent years. Early studies examined specific disk heating mechanisms such as heating by dissipationless mergers of satellites (Toth & Ostriker 1992, Quinn, Hernquist & Fulagar 1993, Velazquez et al 1999) or dissipative accretion of gas-rich stellites orbiting in the same plane as the main disk (Bekki & Chiba 2001, Brook et al 2004). This was followed by an era where thick disk and halo formation processes were examined in hydrodynamical zoom simulations of individual galaxies, where the accretion processes follow the expectations of dark matter halo assembly in a Λ CDM cosmology (Brook et al 2012, Abadi et al 2013)

Most recently, it has been noted that thick disk formation processes can differ substantially depending on the physical treatment of star formation and supernova/AGN feedback processes. For example, Yu et al (2021) have studied thick stellar disc formation in Milky Way-mass galaxies using 12 FIRE-2 cosmological zoom-in simulations and show how that most of the mass is formed during periods of bursty star formation when supernova-driven outflows drive a large amount of gas out to large distances above the galactic plane. Pinna et al (2024) analyzed thick disk assembly in the AURIGA simulations and found that there is early in situ formation, but there is later growth driven by the combination of direct accretion of stars from satellite infall, some in situ star formation fueled by mergers, and dynamical heating of stars. Elias et al (2018) have also noted that there is substantial scatter from one halo to another within one simulation set and this has been verified observationally for Milky Way mass galaxies (Merritt et al 2016). This means large samples of galaxies are crucial in making fair comparisons between simulations and data.

We note that there have been almost no studies that have used IFU data to carry out a combined analysis of the stellar and ionized gas properties of the same galaxies. In this paper, we analyze a sample of 82 edge-on disk galaxies drawn from the Mapping Nearby Galaxies at APO (MaNGA survey). We stack the spectra as function of vertical scale height above/below the disk and we are able to trace the stellar light distribution out to typical distances of 10 kpc. As we will show, this is usually far enough to measure the radius at which the stellar light profiles start to flatten because of the increasing contribution of light from the stellar halo (Gilhuly et al 2022). We are also able to measure 4000 Å break profiles out to distances of 4-6 kpc above and below the disk as a probe of stellar population age, and strong emission lines [OII] λ 3727 and H α as a probe of the ionized gas. The goal is to study the correlations between the properties of the extra-planar stars and gas with the properties of the main galaxy, such as mass, bulge-to-disk ratio and specific star formation rate, as well as to understand how the extra-planar components correlate with each other. Although this sample is not extremely large, we will show

that it is sufficient to examine trends in the two-dimensional space of galaxy stellar mass and star formation rate.

Our paper is organized as follows. In section 2, we describe the selection of the galaxy samples used in the analysis. In section 3, we describe the methodology used for creating stacked spectra and deriving profiles for quantities pertaining to the stellar light and to extra-planar ionized gas. Results are presented in Section 4 and are summarized and discussed in Section 5.

2 THE GALAXY SAMPLE

We use the final version of the MaNGA data (Abdurro'uf et al. 2022). MaNGA was a survey carried out as part of the SDSS-IV survey (Sloan Digital Sky Survey) using IFU observations of galaxies to produce spatially resolved spectroscopic data (Gunn et al. 2006; Bundy et al. 2015; Drory et al. 2015; Blanton et al. 2017; Aguado et al. 2019; Abdurro'uf et al. 2022). MaNGA observed approximately 10,000 galaxies, selected as an unbiased sample in terms of stellar mass over the range $M_* > 10^9 M_\odot$ and environment (Law et al. 2015; Yan et al. 2016; Wake et al. 2017). The primary sample in MaNGA consists of about 5000 galaxies selected with IFU coverage out to $1.5R_{eff}$. The secondary sample of the main subgroups includes about 3300 galaxies, observed by the IFU bundle out to $2.5 R_{eff}$.

The IFU bundles of the MaNGA survey consist of 19-127 fibres with hexagonal shape covering 12-32 arcseconds in diameter on sky. The spatial resolution of MaNGA is 2.5 arcsec, which corresponds to 1.3-4.5 kpc for the primary sample and 2.2-5.1 kpc for the secondary sample. The BOSS spectrographs used by MaNGA provide spectra from 3600 to 10300 Å with a spectral resolution $R \sim 2000$ (Smee et al. 2013; Yan et al. 2016). The observations were conducted to reach a signal-to-noise ratio (S/N) in the stellar continuum of 14-35 per spatial sample, which required about 3 hours net integration for each target.

In this paper, we focus on a sample of 82 edge-on disk galaxies selected from the MaNGA sample. As discussed in Beom et al (2022), selection of suitable samples of edge-on galaxies requires two main steps. First, stellar masses and structural parameters such as position angles, ellipticities, and half-light radii for all galaxies in the MaNGA sample are available from the MaNGA drpall file; in all cases, the structural parameters are obtained from the SDSS elliptical Petrosian apertures. In the initial cut, all galaxies with major-to-minor axis ratio b/a less than 0.35, Sersic indices less than 2.5, redshifts greater than 0.01 and stellar masses in the range $10^8 < M_* < 10^{11} M_\odot$ are selected. This results in a sample of 481 galaxies. The second step involves visual inspection of the images to find those objects where the IFU covers most of the disk, and where there are no bright stars or galaxies in the vicinity where scattered light could contaminate the off-axis measurements of flux from the galaxy. In addition, we eliminate merging galaxies and galaxies in dense environments such as groups and clusters where it would be difficult to disentangle the low surface brightness emission from different systems. These cuts are fairly stringent and result in a sample of 68 galaxies. A gallery of g, r, i cut-out images is shown in Figure 1. The galaxies are ar-

ranged in order of increasing stellar mass and the purple hexagons show the spatial coverage of the MaNGA IFU.

The sample cut on Sersic index and b/a is designed to select only edge-on, disk-dominated galaxies for study. In Figure 2, we plot the distribution of b/a in bins of stellar mass and find that these are almost identical, indicating that our cut is selecting a morphologically uniform population of objects. In order to quantify the effect of a more prominent bulge component on the properties of the thick disk and the inner halo, we eliminate the cut on Sersic index and visually examine all galaxies with $b/a < 0.40$ and Sersic index greater than 2.5. We find that most systems are irregular/merging objects or galaxies with a central bulge where the disk is not edge-on. We are able to extract a sample of 14 relatively “clean” edge-on galaxies with larger central light concentration for comparison with the main sample of 68 galaxies. A gallery of images from this sample arranged by stellar mass is shown in Figure 3. Our final sample thus consists of a total of 82 edge-on galaxies.

3 ANALYSIS METHODS

The primary MaNGA data products are composed of 3-D calibrated data cubes produced by the data reduction pipeline (DRP). In this section, we discuss how we combine spectra from the MaNGA cube file to calculate the stellar light and $D_n(4000)$ break profiles of the galaxies in our sample, as well as average emission line strengths in the thick disk and inner halo.

We work with the SPX-MILESHC-MASTARSSP LOGCUBE and MAPS files, which contain spectra and analysis products for each individual spaxel with $S/N > 1$. The orientation of the edge-on thin disk is determined from the g -band weighted mean flux (SPX-MFLUX) measurements for each spaxel. We perform successive least squares linear fits to subsets of the spaxels, starting from the 10% brightest central spaxels, and then including fainter and fainter spaxels iteratively.¹ During each fitting procedure, we calculate the position angle of enclosed light using the linear fit, as well as maximum radial extent from the central spaxel.

The reason the iterative procedure is needed, is because many galaxies have inner light concentrations that are misaligned with the more extended region of the disk. As fainter and fainter spaxels are included, the fit will start to orientate with the low surface brightness light away from the disk and the maximum radial extent of the spaxels will no longer increase significantly. The iterative fitting procedure almost always converges to a stable estimate of the orientation of the disk in a region where the maximum radial extent is still increasing on each iteration, but the estimated disk position angle remains fixed.

The next step is to create stacked spectra as a function of perpendicular distance from the disk. We create median stacked spectra in order to reduce the influence of outliers and we estimate the error on the median using a standard bootstrap error estimation method with 100 replications. Our stellar continuum flux estimation is carried out over the

¹ The central spaxel is always defined using the MaNGA coordinate system as given in the Data Analysis Pipeline.

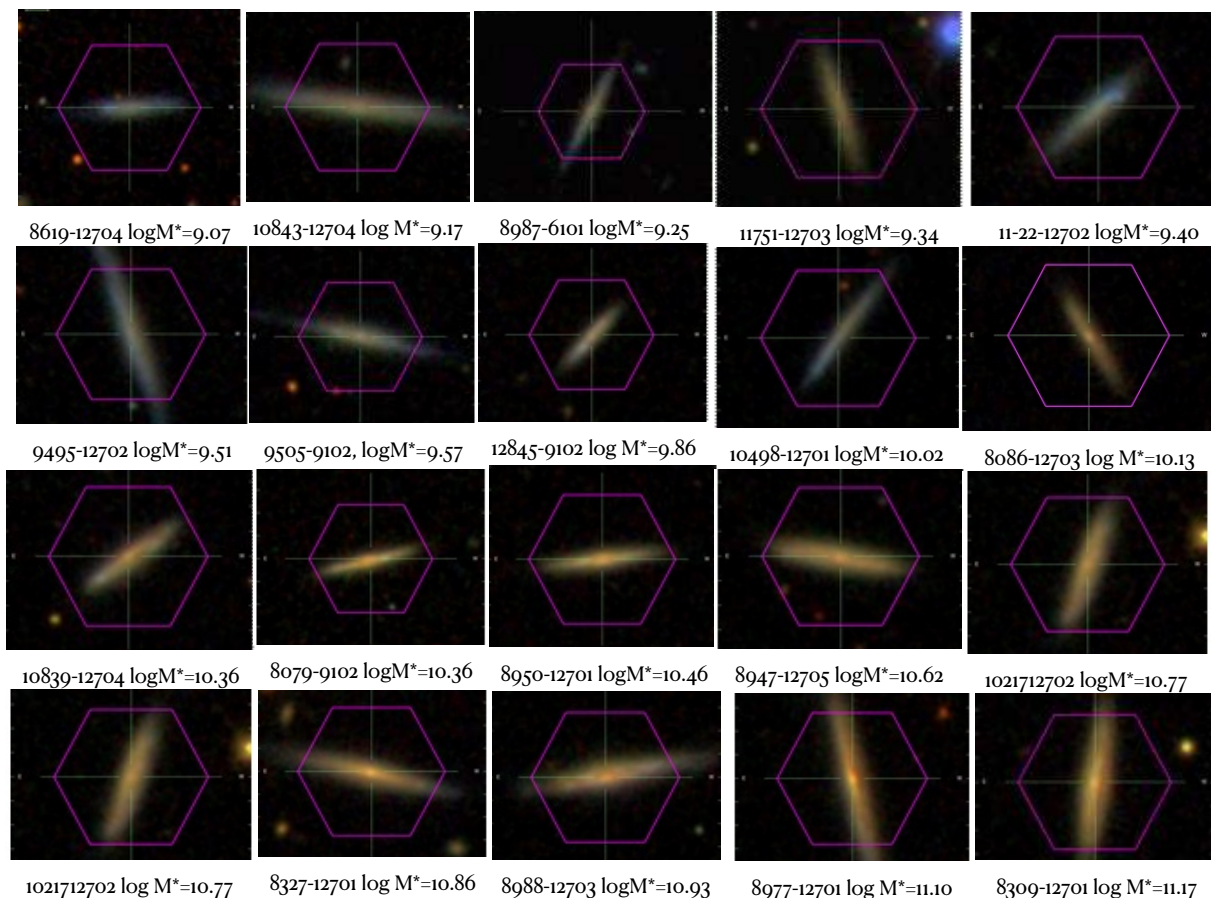


Figure 1. A gallery of g, r, i -band cutout images of edge-on galaxies from the sample with Sersic index less than 2.5 is shown. The galaxies are arranged in order of increasing stellar mass. Each image is labelled with its MaNGA-id numbers and its stellar mass.

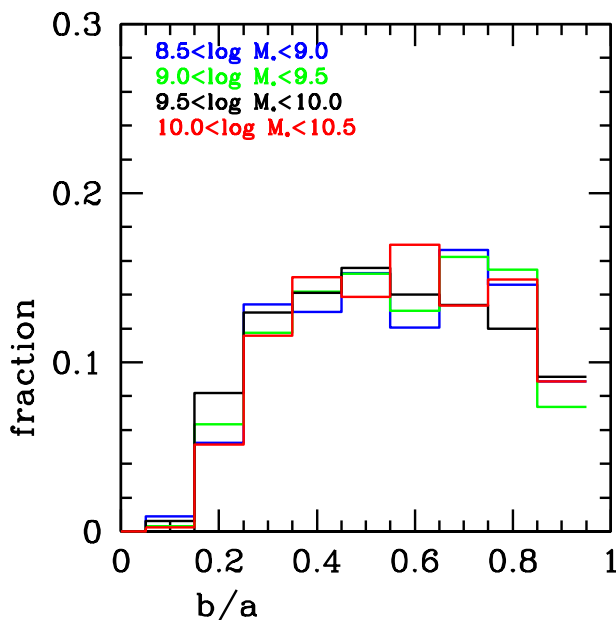


Figure 2. The distribution of b/a in bins of stellar mass in the parent sample.

wavelength interval from 5015 to 6290 Å. This wavelength range is chosen because it does not contain any strong emission lines and it is also in the region of the spectrum with highest S/N . The spectra are arranged in order of increasing perpendicular distance from the disk and the stack is first carried out in bins of 20 spectra at a time. If the S/N in the continuum flux is less than 70, more spectra are added to the stack until $S/N = 70$ is reached. The stacking process is stopped once there are no more spectra left to stack, or the S/N of the stack falls below 10.

In Figure 4, we show the profiles for the same disk-dominated galaxies pictured in Figure 1. The logarithm of the average flux per spaxel is plotted as a function of distance from the disk plane in units of kiloparsec. The cyan shaded region shows the error estimate on the flux. As can be seen, the outer disk profiles of low mass galaxies (top and second rows) are well-characterized by a steeply declining power-law. In some cases, the profile appears to break or flatten. As the stellar mass of the galaxy increases, the outer disk profiles have a shallower slope and a flattening at large radius is clearly found in almost all galaxies (third and bottom rows). We will describe how we place the profile trends on quantitative footing through profile fitting in the next section.²

² The profiles of the sub-sample with Sersic index greater than 2.5 are quite similar in terms of basic trends such as slope of the

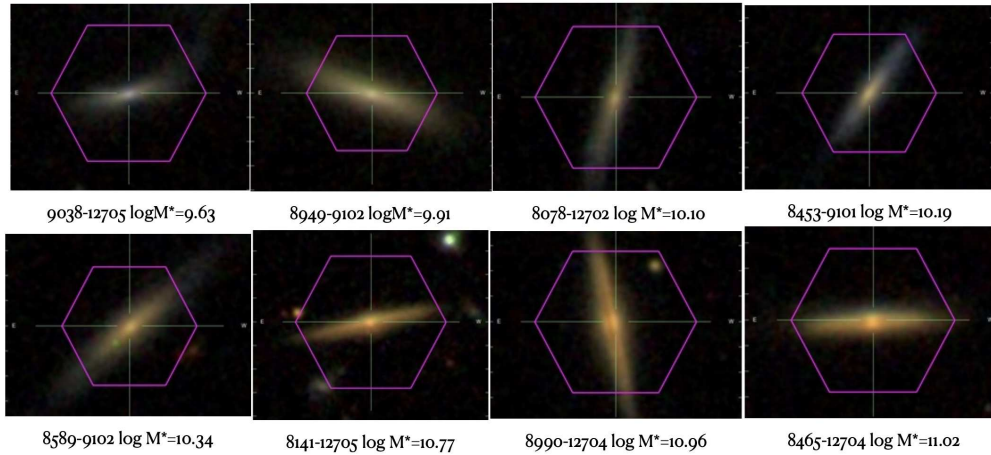


Figure 3. Same as Figure 1, except for galaxies with Sersic index greater than 2.5.

We also calculate the 4000 Å break index $D_n(4000)$ and plot these as red points with error bars over the range where the error remains smaller than 0.2. $D_n(4000)$ in normal galaxies varies over the range between 1.1 for galaxies with very young stellar populations, where a recent burst of star formation has occurred, to values of 2 for galaxies with old, metal-rich stellar populations (see Kauffmann et al 2003; Kauffmann 2014). As can be seen, our $D_n(4000)$ measurements always fall within this range. The majority of galaxies have $D_n(4000)$ profiles that are flat in the inner disk and then increase in the power-law thick disk region, in agreement with the findings of Dalcanton & Bernstein (2000). In most galaxies, we are not able to obtain a high S/N measurement of the 4000 Å break in the region where the surface brightness profiles flatten. In a few galaxies, the $D_n(4000)$ profiles show a break towards smaller values at large distances and there also may be more than one break in the profile. We will also quantify the $D_n(4000)$ trends in more detail in the next section.

Finally, in order to detect the emission lines in the stacked spectra of the thick disk and halo-transition region at high enough S/N, we stack spectra in 3 regions: 1) the inner disk region where the surface brightness profiles are flat, 2) the thick disk region where the surface brightness profiles are declining with a fixed power law slope, 3) the halo transition region where the surface brightness profiles are flattening. An example of how these stacks are made is shown for the galaxy 10839-12704 in Figure 5. The cyan, red and yellow coloured regions show the regions of the galaxy within 80%, 60-80% and 20-60% of the peak surface brightness. The green, black and red points indicate the positions of the spaxels used to create the stacked spectra in the inner disk, the thick disk and the halo. The resulting spectra are plotted in 4 different wavelength ranges containing the strongest emission lines in Figure 6. The top row of the figure shows the spectral stacks over the wavelength range covering the H α and [NII] lines as well as the [SII] doublet. The second row shows the region covering the high-ionization [OIII]

thick disk profile as function of stellar mass and the flattening in the outer regions, so we do not show a separate plot for these objects.

line. The third and fourth rows cover the lower ionization [OII] and [OI] lines and the bottom row covers the 4000 Å break region of the spectrum.

The stacked spectra plotted in the left columns are for the inner region of the disk seen edge-on, the middle column shows the stacked spectra in the thick disk region and the right column shows the spectra in the transition regions between thick disk and halo. The [OII] and H α emission lines are almost always detected in the thick disk region and also with reasonable frequency in the inner halo. The [OIII] line is almost never detected outside the inner disk. The [OI] line is detected in a small subset of galaxies out to large radius from the disk. In this paper, we will focus on the [OII] and H α lines as tracers of the ionized gas.

Because the spectra in the outer disk regions are very noisy and because the line shapes are quite often complex, we use a non-parametric method to calculate the emission line equivalent widths. We define two continuum bands of width 20Å located symmetrically on either side of the emission line. The adopted continuum bands are located further away from the rest-frame wavelength of the line in the outer disk and in the inner halo stacks, because the emission lines are frequently broader in these regions. We calculate F_{cl} and F_{cr} , the continuum flux on the left and the right side of the lines, along with errors estimated by bootstrap resampling of the spectral measurements. Within the region that is assumed to contain the line emission, we locate the maximum flux point, and then integrate the flux to the left and to the right of this point until it drops below the continuum level by 2σ for the first time. This procedure is repeated 100 times on bootstrap resampled spectra to calculate a median EQW as well as the 16-84th percentile confidence ranges. Our results will be presented in the next section.

4 RESULTS

4.1 Parameters of the stellar light profiles and their scalings

Many past papers on the structure of edge-on disk galaxies have focused on accurate methods for deconvolving the thin and thick disk components. The IFU observations of

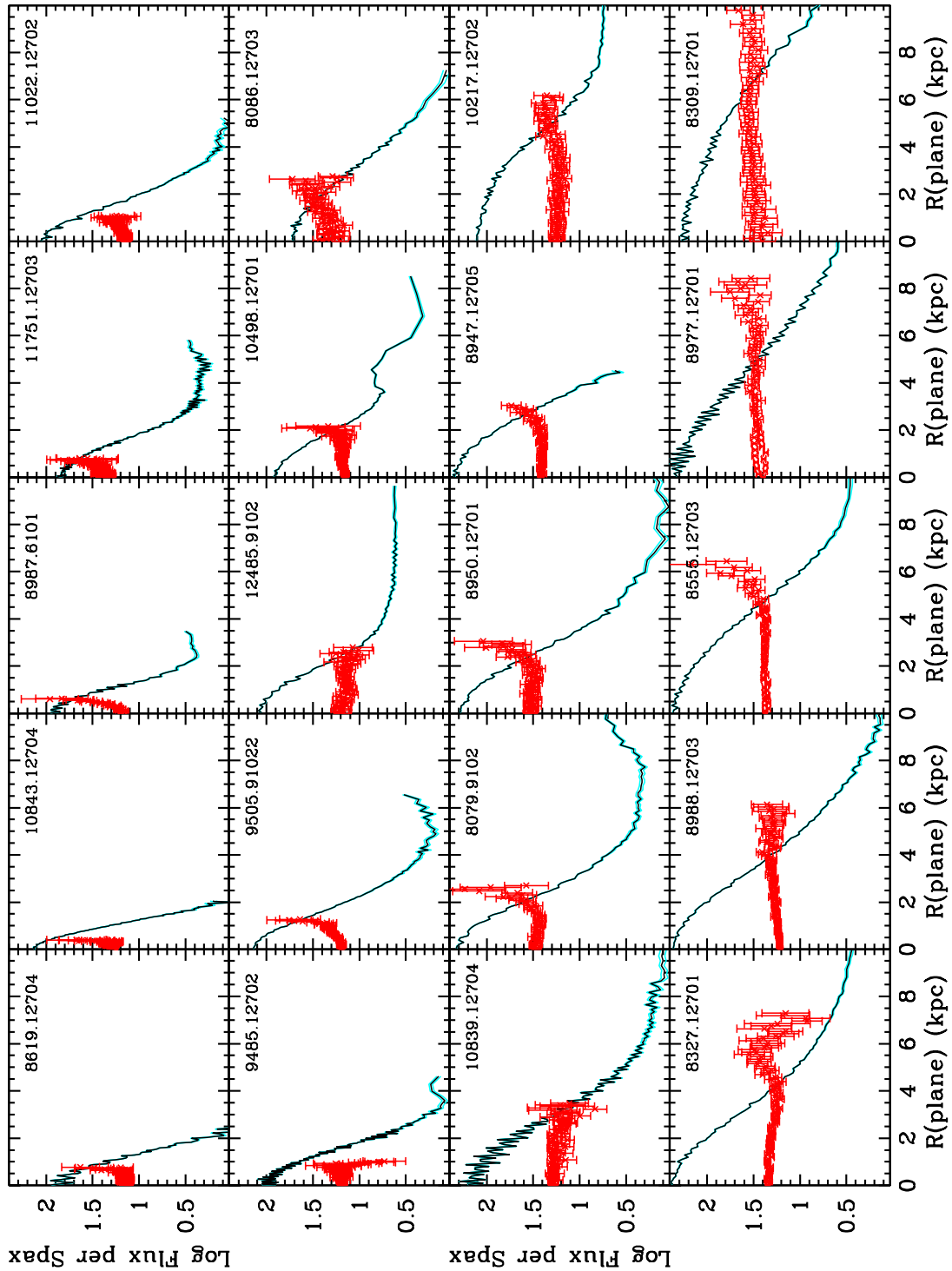


Figure 4. Surface brightness profiles for the same disk-dominated galaxies pictured in Figure 1, arranged in order in increasing stellar mass, from left to right and from top to bottom. The logarithm of the average flux per spaxel is plotted as a function of distance from the disk plane in units of kiloparsec. The cyan shaded region shows the error estimate on the flux. $D_n(4000)$ profiles are plotted as red points with error bars over the range where the error remains smaller than 0.2. Note that the flux units have been scaled so that we are able to show the surface brightness and $D_n(4000)$ profiles using the same values on the y-axis of each panel in the figure.

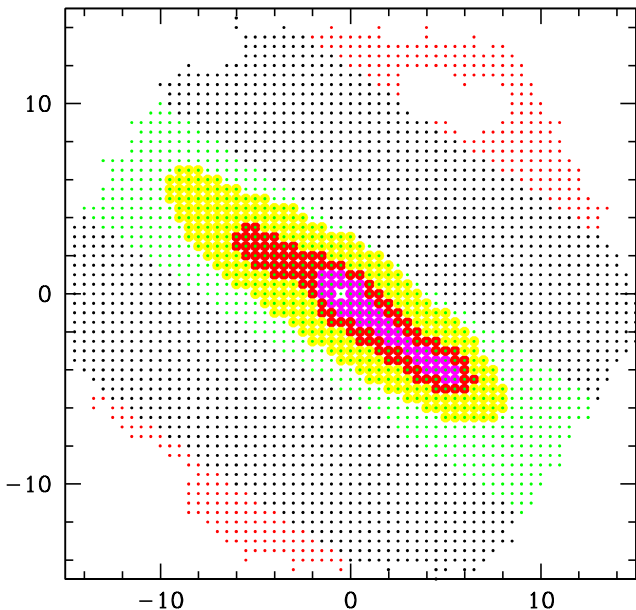


Figure 5. An example of how stacks in the inner disk, the thick disk and the halo are made is shown for the galaxy 10839-12704. The cyan, red and yellow coloured regions show the regions of the galaxy within 80%, 60-80% and 20-60% of the peak surface brightness. The green, black and red points indicate the positions of the spaxels used to create the stacked spectra in the inner disk, the thick disk and the halo, respectively.

edge-on galaxies studied here have limited (~ 1 kpc) spatial resolution and we will not adopt this approach. Rather than attempting a 3-zone decomposition into thin, thick disk and halo components, only a two-zone definition of power law for the thick disk at distances greater than 1-1.5 kpc above the plane and flattening for the stellar halo is made.

As discussed in the previous section, the average surface brightness profiles as a function of perpendicular distance to the disk plane are well-characterized by a power-law region that extends from ~ 1 kpc to typical distances of 3-7 kpc, before flattening. We will thus parametrize these profiles with two quantities: 1) The slope b in the power-law part of the profile, 2) R_{break} , the break radius, where the profile lies more than 3σ above the best-fit power law for four successive radial bins.

In Figure 7, we show how these two profile parameters depend on the stellar mass and the logarithm of the specific star formation rate $\log SFR/M_*$ for 82 galaxies in our sample. The disk-dominated galaxies are plotted as black circles, while the sample with higher Sersic indices are plotted as red triangles. In these plots, we have used stellar masses and star formation rates from the MaNGA Pipe3D value-added catalog of spatially resolved and integrated properties of galaxies for DR17 (Sanchez et al 2022; Lacerda et al 2022). We use the integrated stellar mass derived from fitting the MILES stellar population synthesis model outputs (Vazdekis et al 2010) to spectra from each spaxel to obtain the local stellar surface density Σ_* and then integrating the local stellar surface density estimates to obtain the total stellar mass. The total star formation rates are

estimated in a similar way using the $H\alpha$ emission line luminosities, corrected for dust extinction using the value of the Balmer decrement $H\alpha/H\beta$. The stellar mass estimates from the Pipe3D catalogue tend to be systematically higher by 0.1-0.2 dex because the contribution from lower surface brightness regions of the galaxy are included. Error bars on the slope and R_{break} parameters are calculated by adding noise to the profiles according to the flux errors calculated by bootstrapping the spaxels considered in each radial bin. The error bars on the slope are smaller than the size of the plotted symbols and cannot be seen. Some of the errors on R_{break} are more substantial and can be seen in the figure.

Figure 7 shows that there is a tight scaling between R_{break} and slope b for galaxies in the stellar mass range $10^9 - 10^{10} M_\odot$. The Pearson correlation coefficient R has a value of 0.73 with an associated p-value of 3.85×10^{-5} . Above this stellar mass, there is no longer a strong correlation between profile parameters and stellar mass ($R=0.11$ and $p=0.37$), and the scatter at fixed M_* also increases.

The association of the R_{break} with the transition from the thick disk to the halo component is very clearly demonstrated in recent work by Gilhuly et al (2022) analyzing 12 nearby edge-on galaxies from the Dragonfly Edge-on Galaxies Survey (DEGS). These observations reached limiting g and r -band surface brightnesses of 32 mag/arcsec^2 , allowing the stellar light to be probed out to distances of 20-60 kpc from the disk plane. These authors constructed surface brightness profiles from elliptical isophote fitting as well as profiles as a function of distance along the minor axis, as done in this paper. The minor axis profiles shown in Figure 9 of Gilhuly et al show a steep inner power-law region and a clear flattening that begins at similar radii as found in this analysis.

As noted by Gilhuly et al (2020), the profile breaks seen in edge-on galaxies can only be used as a very approximate indicator of a transition from the star-forming disk to a “pure” stellar halo consisting of stars accreted during the hierarchical assembly of the surrounding dark matter halo. Studies of the stellar mass surface density profiles of 17 Milky Way-mass galaxies from the FIRE-2 suite of simulations by Sanderson et al. (2018) found no threshold or inflection point that consistently indicated a transition to an accretion-dominated regime. This was directly attributed to the natural variety among accretion histories and therefore the amount and distribution of accreted stars with respect to stars that were formed “in situ” from gas in the disk. The large observed scatter in R_{break} as a function of stellar mass of the galaxy that we find in the Milky Way mass range is quite consistent with these simulation predictions.

At stellar masses less than $10^{10} M_\odot$, we find that R_{break} increases as a function of M_* and there is a significant correlation between these quantities ($R=0.566$, $p = 3.95 \times 10^{-3}$). This could be an indication that the relative contribution of the accreted component is smaller for lower mass galaxies. Wang & Kauffmann (2008, see Figure 3) use semi-analytic models implemented within the Millennium simulation to show that fraction of galaxies that have not experienced either major or minor mergers increases strongly at stellar masses less than $10^{10} M_\odot$.

Finally, the lack of correlation between the profile parameters and the star formation activity in the disk, as indicated by $\log SFR/M_*$ is also an indication that these

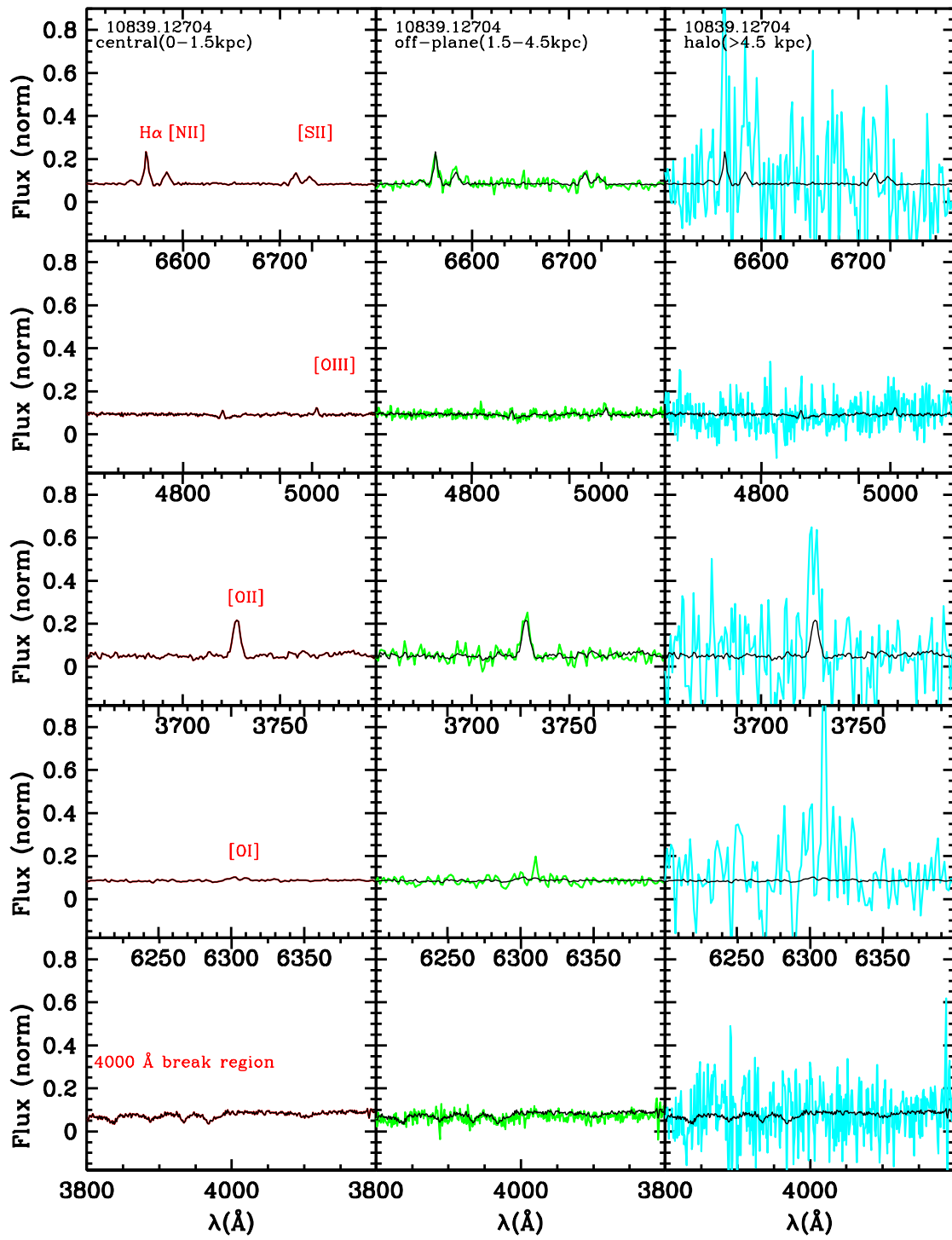


Figure 6. Stacked spectra for the galaxy 10839-12704 in 4 different wavelength ranges containing the strongest emission. The top row of the figure shows the spectral stacks over the wavelength range covering the H α and [NII] lines as well as the [SII] doublet. The second row shows the region covering the high-ionization [OIII] line. The third and fourth rows cover the lower ionization [OII] and [OI] lines and the bottom row covers the 4000 Å break region of the spectrum. The columns show spectra in 3 regions: 1) the inner disk region where the surface brightness profiles are flat, 2) the thick disk region where the surface brightness profiles are declining with a fixed power law slope, 3) the halo transition region where the surface brightness profiles are flattening. The black spectrum that is shown in all panels is the inner disk spectrum, while the red green and cyan spectra are for inner dis, thick disk and halo.

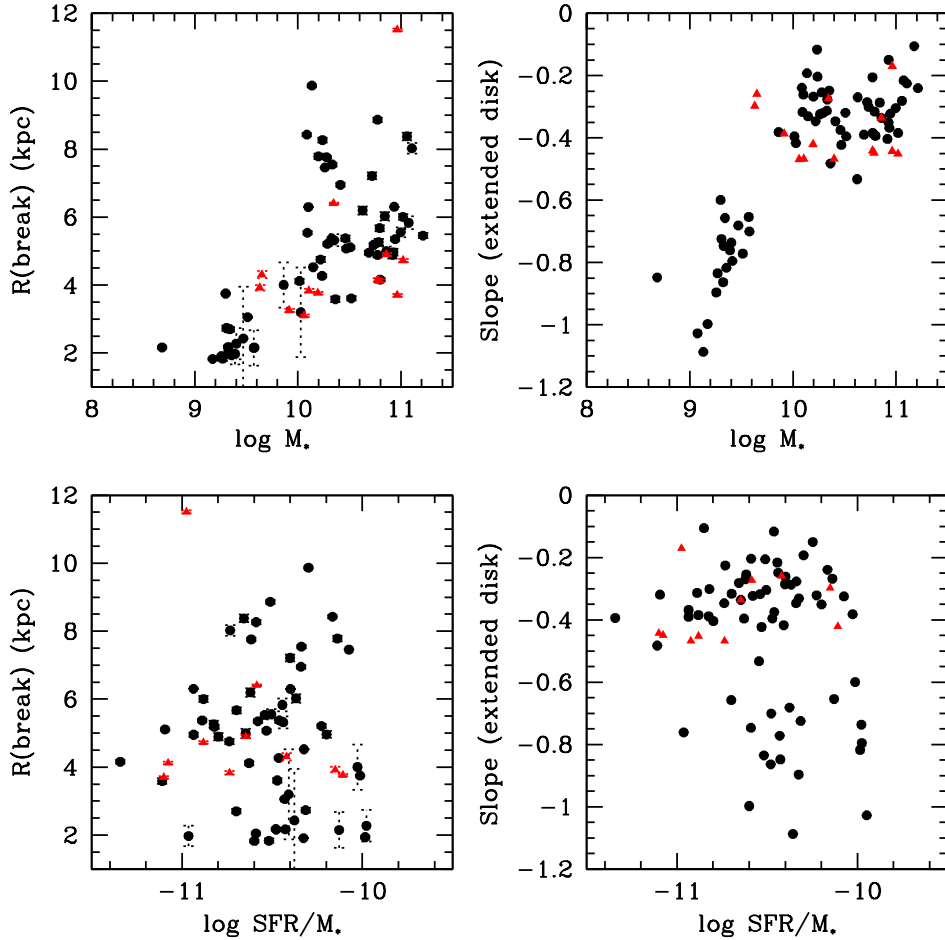


Figure 7. The two thick disk profile parameters slope b and break radius, R_{break} , are plotted as a function of the stellar mass and the logarithm of the specific star formation rate $\log SFR/M_*$ for 82 galaxies in our sample. The disk-dominated galaxies are plotted as black circles, while the sample with higher Sersic indices are plotted as red triangles.

parameters are not determined by present-day gas-physical processes in the disk.

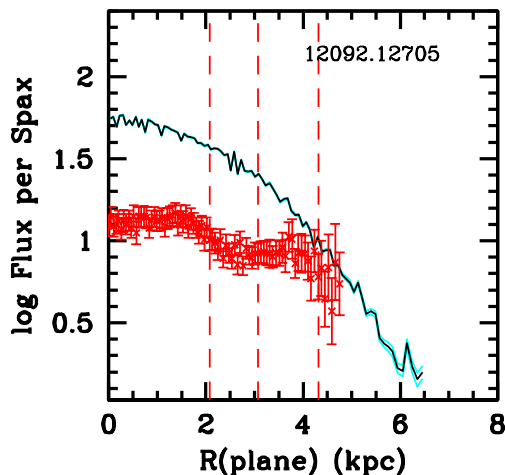
The majority of the subsample of galaxies with higher Sersic indices, indicated by the filled red triangles in Figure 7 have stellar masses greater than $10^{10} M_{\odot}$ and have profile parameters that overlap those of the disk-dominated edge-on galaxies. Only two galaxies in the higher Sersic index sample have stellar masses $\sim 10^{9.5} M_{sol}$ and interestingly, these have extended disk profiles with much shallower slopes than more disk-dominated edge-on galaxies of the same mass. This may indicate that the same process that created the bulge was responsible for creating a more extended thick disk with a shallower light profile. Larger samples of low mass edge-on galaxies are needed to confirm this conjecture.

4.2 4000 Å break profiles

Our analysis of the 4000 Å break profiles begins with a linear fit to the $D_n(4000)$ measurements within a distance of 1.5 kpc from the disk plane. A “break” in the profile is defined as the first time one of two conditions are satisfied:

- 1) Four successive $D_n(4000)$ measurements lie more than 3σ away from the inner disk fit,
- 2) One measurement lies more than 3σ away from the inner disk fit, and the next three $D_n(4000)$ measurements exhibit increasing deviation from the fit. The first condition identifies breaks in regions of the profile with high S/N $D_n(4000)$ measurements, while the second criterion is designed for lower S/N outer region measurements. Once a break is identified, a new linear fit is carried out starting with measurements more than 0.6 kpc from the breakpoint, and a new break-finding procedure is restarted. In Figure 8, we show an example of a galaxy where three breaks are identified in the $D_n(4000)$ profiles, with the position of each break indicated by red vertical lines on the plot.

We define $D_n(4000)(inner)$ as the average $D_n(4000)$ value within the inner 1.5 kpc region of the galaxy, and $D_n(4000)(outer)$ as the average $D_n(4000)$ value in the region starting from the last break point to 0.6 kpc beyond the break point. The quantity $D_n(4000)(outer) - D_n(4000)(inner)$ provides a measure of the gradient in age of the stellar population. We also record the quantity N_{break} , the number of



An example of a galaxy where three breaks are identified in the $D_n(4000)$ profiles, with the position of each break indicated by red vertical lines on the plot.

break points in the $D_n(4000)$ profile, as a measure of the irregularity in the stellar population distributions in the outer disk and halo transition regions.

The two upper panels of Figure 9 show the relation between $D_n(4000)(\text{inner})$ and the stellar mass and specific star formation rate of the host galaxies. There is a strong correlation with SFR/M_* ($R=-0.72$, $p=10^{-14}$), and a weaker one with M_* ($R=0.50$, $p=1.5 \times 10^{-6}$), reflecting the fact that less massive disk-dominated galaxies have younger stellar populations. For edge-on galaxies, dust extinction effects may also play a secondary role in increasing the measured value of $D_n(4000)$ at fixed stellar age, but we note that we use the narrow version of the index that is measured within 100 \AA wide windows, so the effect of dust is minimized. Edge-on galaxies with higher Sersic indices (plotted as red triangle) exhibit somewhat more scatter in the top panels of Figure 9, but otherwise follow the same correlation defined by the more disk-like edge-on galaxies.

In the bottom left panel, we plot $D_n(4000)(\text{outer}) - D_n(4000)(\text{inner})$ as a function of the stellar mass of the galaxy. The numbers in the left-hand part of the figure indicate (from top to bottom) the number of galaxies where this quantity is positive, zero (indicating a flat profile with no breaks) and negative. The numbers in parentheses are for the high Sersic index sample. The results indicate that the 4000 \AA break profiles are flat or positive for 85% of the sample, indicating that for the majority of galaxies, the extended disk regions contain stars that are as old or older than those in the inner disk. These results are the same for the pure disk and for the high Sersic index samples. The quantity that differs significantly between the disk and the bulge samples is the distribution of N_{break} , the number of break points in the $D_n(4000)$ profile (plotted in the bottom right panel of Figure 9). 40% of the pure disk edge-on galaxies have no breaks in their $D_n(4000)$ profiles, whereas only 1 out of 14 galaxies in the high Sersic index sample has no breaks. More than a third of the high Sersic index sample has 2 or more breaks, whereas only 12% of the disk sam-

ple have this many breaks. As we will discuss in more detail later, the fact that the number of breaks correlates with the morphological type of the galaxy and also the fact that they occur most often at large extra-planar distances, may argue for a merger/accretion origin.

We now split the sample into galaxies with positive/zero values of $D_n(4000)(\text{outer}) - D_n(4000)(\text{inner})$ and negative value of this quantity. Histograms of the stellar mass, the specific star formation rate of the galaxies, as well as the slope b of the power-law component of the extended disk are plotted in the top row of Figure 10. The black histograms are for the galaxies with flat $D_n(4000)$ profiles and the blue histograms are for the galaxies where the stellar populations become younger in the outer disk. As can be seen, there is no statistically significant difference between the two subsamples. In the bottom panels the sample is split according to N_{break} , with black histograms for galaxies with no breaks and red histograms for galaxies with one or more breaks. Here it can be seen that galaxies with breaks have higher stellar masses and shallower outer disk slopes.

4.3 Emission line properties in the outer disk and halo transition regions

Figures 11 and 12 show the equivalent widths of the [OII] and $H\alpha$ emission lines plotted as a function of stellar mass (Figure 11) and $\log SFR/M_*$ (Figure 12). The results are plotted for the inner disk stacked spectra (left column), the extended disk stacked spectra (middle column) and the halo transition region stacks (right column). There is no strong correlation between [OII] and $H\alpha$ equivalent widths and stellar mass in any of the three regions. There is a weak tendency for the most massive galaxies to have slightly weaker emission lines. Figure 12 shows that the emission line equivalent widths in all three regions correlate with the specific star formation rate of the galaxy. The correlation in the halo transition region is somewhat clearer for the $H\alpha$ line than for the [OII] line.

Similar to the analysis in the previous section, we split the sample into galaxies with positive/negative values of $EQW(H\alpha)(\text{outer disk}) - EQW(H\alpha)(\text{inner disk})$ and $EQW([OII](\text{outer disk}) - EQW([OII](\text{inner disk}))$ and plot histograms of galaxy properties. The results are shown in Figure 13. In the previous section, we found that the distribution of stellar masses and specific star formation rates was the same for galaxies split according to 4000 \AA break gradient. Here we find that more massive galaxies and galaxies with low values of SFR/M_* are more likely to have lower $H\alpha$ EQW in the outer disk compared to the inner disk. The same trend is not found for $EQW [OII]$.

In Figure 14, we explore how the the $[OII]/H\alpha$ ratio changes from the inner to the outer disk in more detail. In the top left panel in the figure, we plot $[OII]/H\alpha$ in the outer disk as a function of $[OII]/H\alpha$ in the inner disk. The dashed line indicates the one-to-one linear relation. Outer disk values are frequently, but not always larger than the inner disk values. In the next two panels, we plot the ratio of outer-to-inner $[OII]/H\alpha$ values as a function of the stellar mass and the specific star formation rate of the galaxy. The results in these two panels confirm that a large increase in $[OII]/H\alpha$ in the outer disk is found in massive galaxies with low specific star formation rate. It is thus unlikely that shocks due to

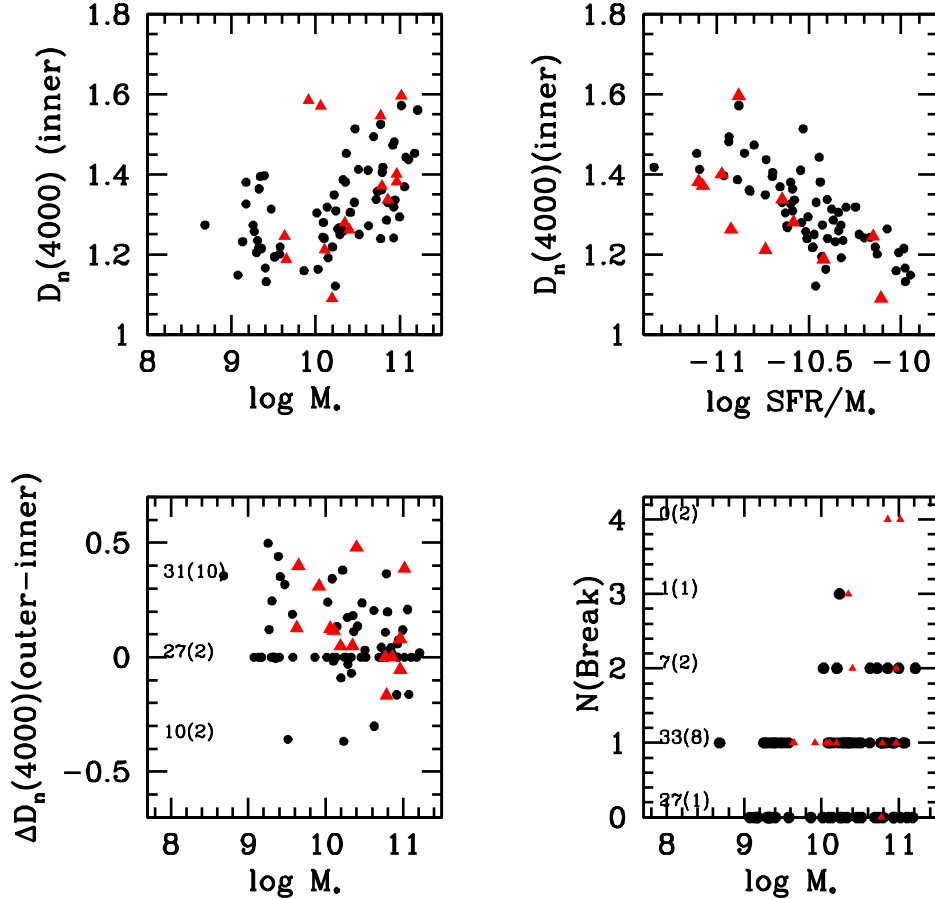


Figure 8. The two upper panels show the relation between $D_n(4000)(\text{inner})$ and the stellar mass and specific star formation rate of the host galaxies. The bottom left panel shows $D_n(4000)(\text{outer}) - D_n(4000)(\text{inner})$ as a function of the stellar mass of the galaxy. The numbers in the left-hand part of the figure (from top to bottom) indicate the number of galaxies where this quantity is positive, zero (indicating a flat profile with no breaks) and negative. The numbers in parentheses are for the high Sersic index sample. The bottom right panel shows $N(\text{Break})$ as a function of the stellar mass. The numbers in the left-hand part of the figure indicate the number of galaxies where this quantity is 0,1,2,3 and 4, with the number in parentheses for the high Sersic index sample.

supernovae-driven outflows or infalling cold gas is responsible for this pattern of ionization. In the bottom panels, we test whether the ratio of outer-to-inner disk $[\text{OII}]/\text{H}\alpha$ values depends on the properties of the outer disk. The bottom left panel shows that large increases in $[\text{OII}]/\text{H}\alpha$ ratio occur in galaxies with extended thick disks (larger values of the slope parameter b). A shallow slope is indicative of a higher fraction of stars located external to the thin disk. The next panel shows that if the 4000 Å break strength decreases in the outer disk, the outer $[\text{OII}]/\text{H}\alpha$ ratios also decrease. Conversely, most galaxies with increasing 4000 Å break values have increasing values of $[\text{OII}]/\text{H}\alpha$.

In summary, the observational data support the hypothesis that ionizing radiation from evolved stars is responsible for the increasing $[\text{OII}]/\text{H}\alpha$ values away from the mid-plane of the galactic disk in massive galaxies.

5 SUMMARY AND DISCUSSION

We have studied the stellar light, 4000 Å break and emission line profiles of a sample of 82 edge-on galaxies from the MaNGA survey. We characterize the stellar light profiles perpendicular to the disk plane using two parameters: a) the power-law slope of the thick disk component, 2) the break radius where the profile flattens. We do not attempt to deconvolve the thin and thick disk components of the galaxy because of the limited spatial resolution of the MaNGA IFU spaxel sampling.

We characterize the 4000 Å break profiles perpendicular to the disk plane by the number of breaks (defined as significant changes in slope) in the profile and by the change in $D_n(4000)$ from the inner 1.5 kpc region of the disk to the region just beyond the last break. The emission line characteristics of the extraplanar gas are characterized using measurements of $\text{H}\alpha$ and $[\text{OII}]$ EQW from stacked spectra in the thin disk, the power-law thick disk and the halo transition regions.

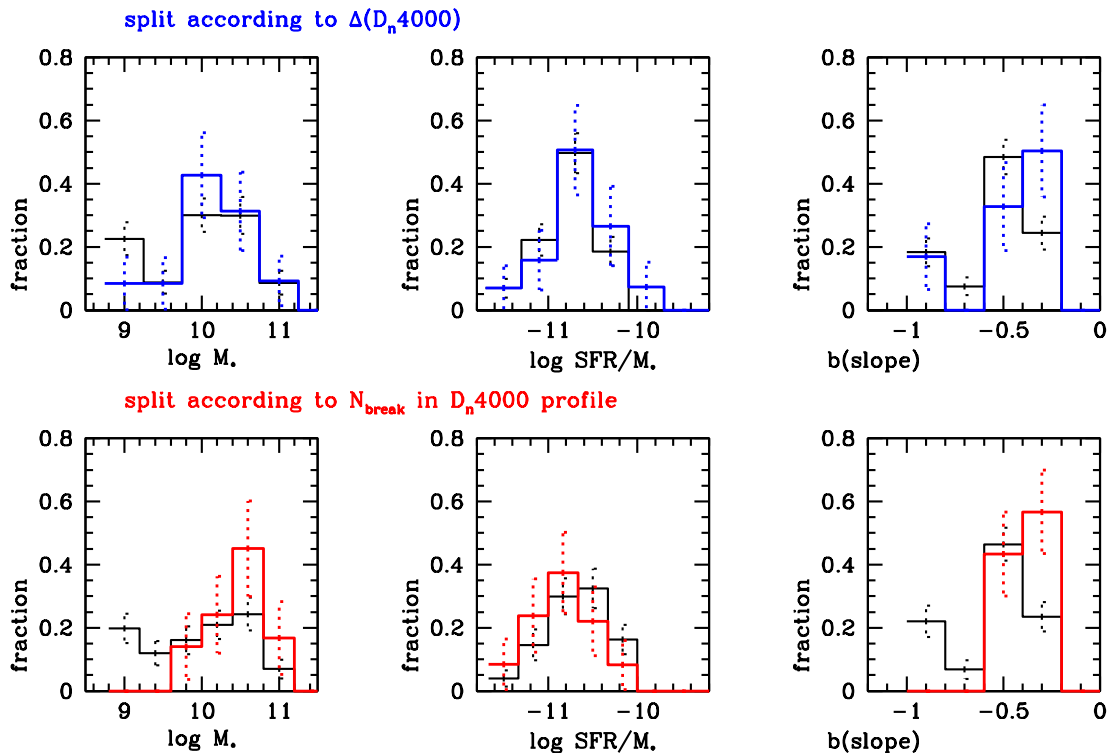


Figure 9. Histograms of the stellar mass, the specific star formation rate of the galaxies, and the slope b of the power-law component of the extended disk are plotted in the top row. The black histograms are for the galaxies with flat $D_n(4000)$ profiles and the blue histograms are for the galaxies where the stellar populations become younger in the outer disk. In the bottom row, black histograms are for galaxies with no breaks and red histograms for galaxies with one or more breaks. Dotted lines show the error bars calculated by bootstrap resampling.

The main results of our analysis are the following:

- Both the slope and the break radius exhibit a tight correlation with the stellar mass of the galaxy over the stellar mass range $10^9 < \log M_* < 10^{10} M_\odot$. At larger stellar masses, both parameters no longer correlate with M_* and also exhibit substantial scatter at fixed M_* .
- 50% of the sample have thick disks with larger values of $D_n(4000)$ than the inner disk. The change in break strength is uniformly spread over values ranging from close to zero to 0.5. 35% of the sample have flat $D_n(4000)$ profiles and 15% of the sample have smaller $D_n(4000)$ values in thick disk. The shift towards lower break values is generally small in these systems. Very “young” thick disk components are thus rare.
- The $D_n(4000)$ profiles exhibit up to 4 separate breaks. The number of breaks is higher in galaxies with larger stellar masses, in galaxies with more extended thick disks and in galaxies with a larger bulge component. We hypothesize that the breaks are produced by accretion events, which have been more frequent in massive galaxies with bulges.
- In contrast, the change in 4000 Å break strength from the inner disk to the outer regions of the thick disk does not correlate with any of the global or structural properties of the galaxy. This may suggest that the accreted satellites that build the thick disk span a wide range in age and/or metallicity.
- In agreement with previous studies, the extraplanar H α EQW correlates most strongly with the specific star forma-

tion rate of the galaxy, and the [OII]/H α ratio increases with distance from the disk plane. This increase is most apparent for the most massive galaxies with the lowest SFR/ M_* and the most extended stellar thick disk components. These findings support the hypothesis that the larger [OII]/H α ratios may be caused by ionization from evolved stars, rather than by other mechanisms such as shocks.

In Figure 15, we show tracks predicted by stellar population synthesis models in the plane of stellar mass-weighted age versus $D_n(4000)$. The blue, black and red curves are for models with 0.25 solar, half solar and solar metallicity. Since the aim is to interpret 4000 Å break measurements for stacked spectra over large spatial scales (7-20 kpc in diameter), we generate models with a continuous star formation history beginning at redshift $z = 5$, with variable e-folding timescale ranging from 0.1-13 Gyr. The population synthesis models are from Bruzual & Charlot (2003) assuming a Kroupa (2001) initial mass function.

We have marked the typical inner disk 4000 Å break strength of 1.4 (see Figure 4) as a solid line. The typical change in $D_n(4000)$ over a break region is around 0.1 (marked as dotted lines on the plot). It can be seen that this corresponds to a shift in mean stellar age of around 1 Gyr. The sensitivity of $D_n(4000)$ to metallicity is quite weak at younger stellar ages. Keeping the stellar age fixed and shifting the metallicity by a factor of two only produces a few percent rather than a ten percent change in the $D_n(4000)$ index. The very largest changes in $D_n(4000)$ from 1.4 in the

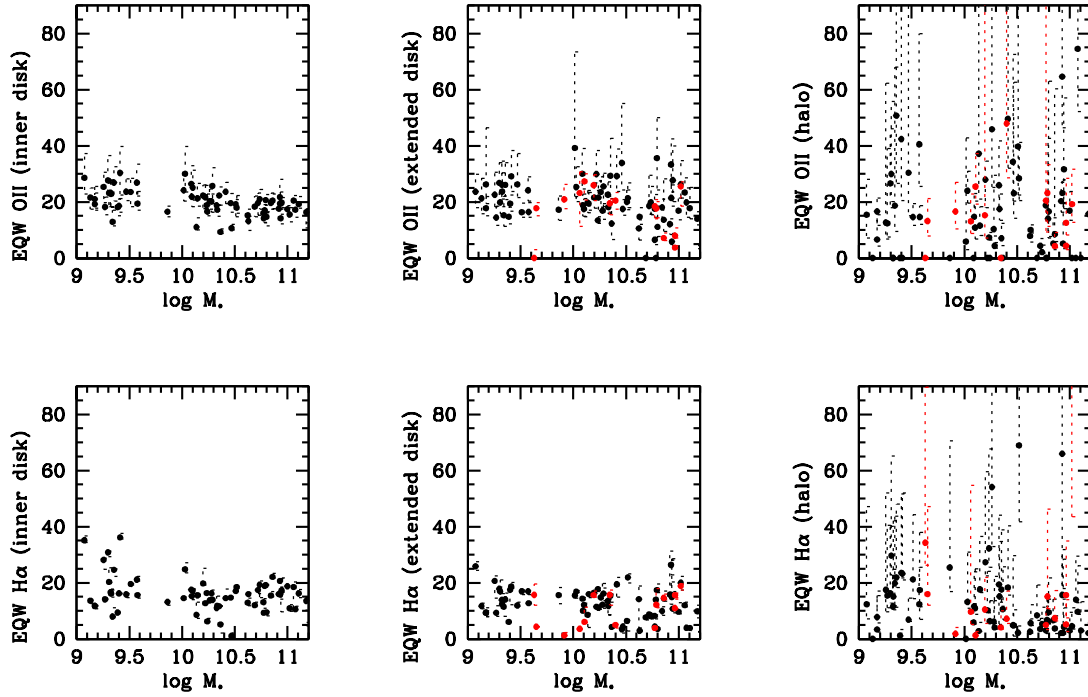


Figure 10. The equivalent widths of the [OII] and H α emission lines is plotted as a function of stellar mass. The results are plotted for the inner disk stacked spectra (left column), the extended disk stacked spectra (middle column) and the halo transition region stacks (right column).

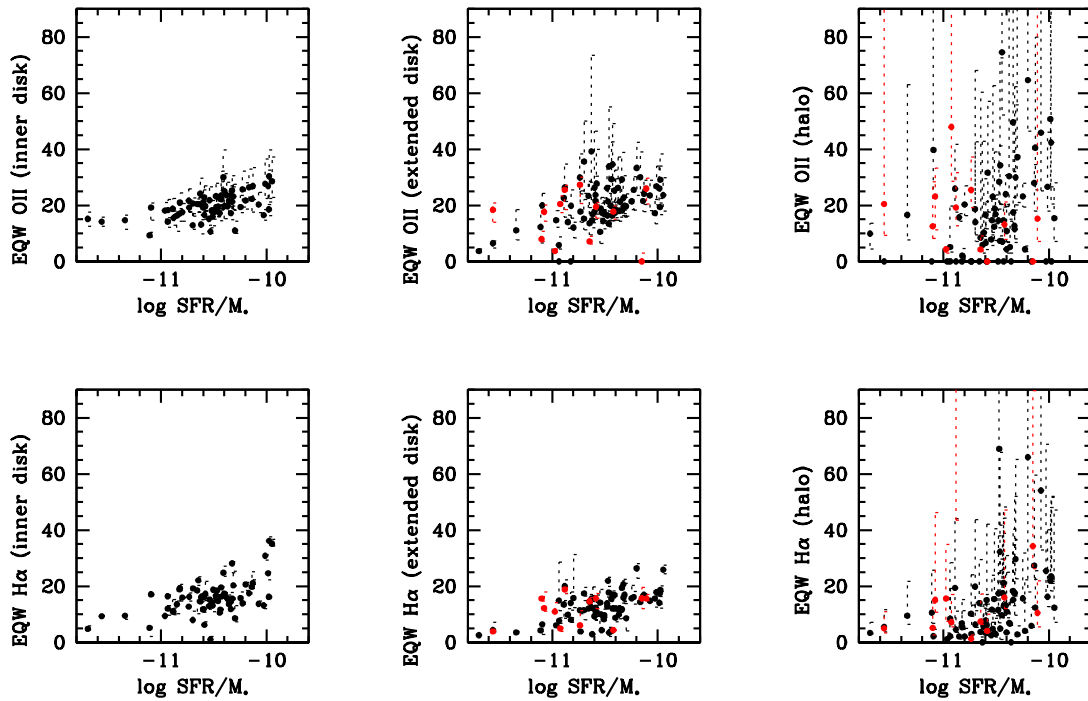


Figure 11. As in the previous figure, except the emission lines are plotted as function of $\log SFR/M_*$.

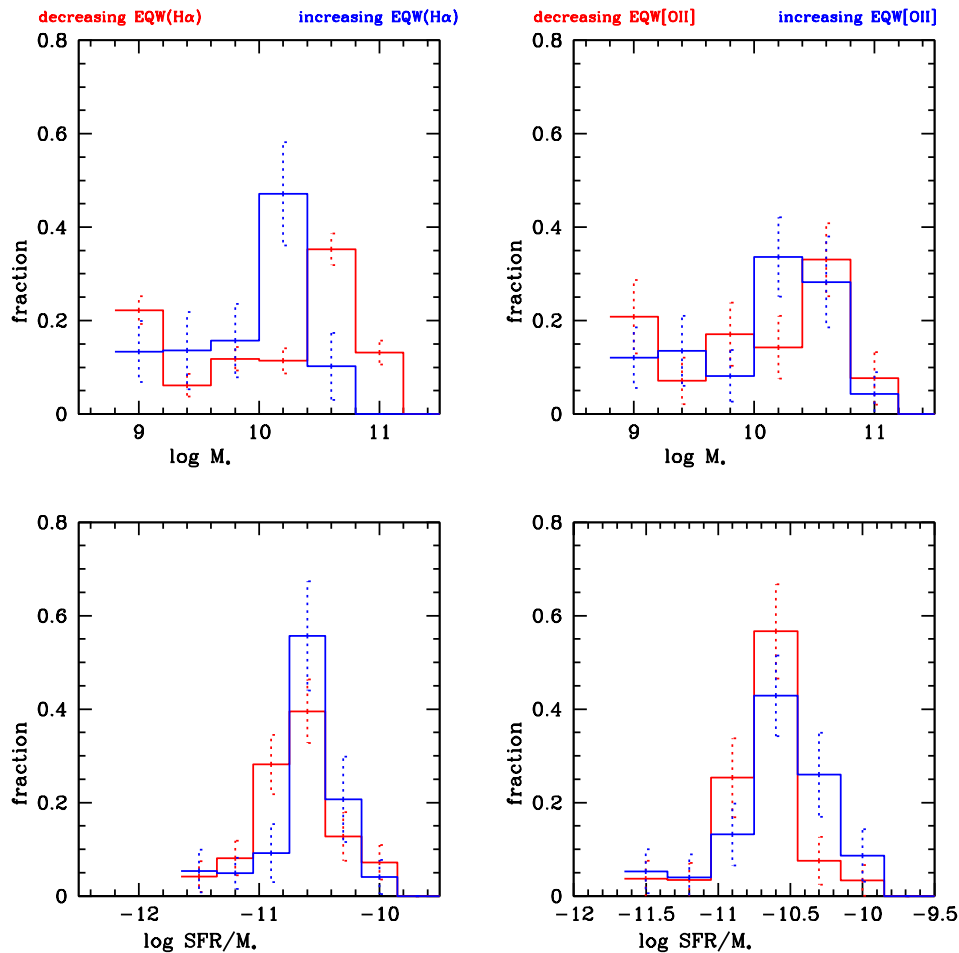


Figure 12. Histograms of galaxy properties for the sample split according positive/negative values of $\text{EQW}(\text{H}\alpha)_{\text{(outer)}} - \text{EQW}(\text{H}\alpha)_{\text{(inner disk)}}$ and $\text{EQW}([\text{OII}]_{\text{(outer)}}) - \text{EQW}([\text{OII}]_{\text{(inner disk)}}$.

inner disk to 1.9 in the outermost regions where the index is still measurable, can be explained by an increase in mean stellar age of around 5 Gyr.

These findings are in good agreement with the results of Sattler et al (2024), who find an average age difference of 2 Gyr between the thin and thick disks of a sample of eight edge-on star-forming disc galaxies observed with the Multi-Unit Spectroscopic Explorer (MUSE). We note that the S/N that we are able to achieve with our stacked MaNGA spectra does not allow us to study metallicity and $[\text{Mg}/\text{Fe}]$ trends as done in this paper.

There are two main physical mechanisms that have been demonstrated to produce thick disks in cosmological simulations of galaxy formation. In N-body simulations that do not include gas, the impact of satellite accretion events that can create thick disks can be assessed by studying the frequency of dark matter subhalo merging events that are aligned with the disk plane. In such studies, the disk plane is assumed to be set by the angular momentum vector of the main halo (e.g. Read et al 2008).

The modern generation of cosmological hydrodynamical simulations are much more successful in producing realistic

Milky-Way type galaxies and it is generally agreed that a combination of gas-physical processes and satellite accretion events can contribute to the build-up of thick disks, with gas-physical processes more important at earlier epochs.

Most of the published work has concentrated on Milky Way mass galaxies. Pinna et al (2024) studied thick disk formation in the AURIGA simulations of 24 Milky Way type galaxies to assess the role played by satellite mergers. They found that mergers contribute an average of 22% of the stellar mass in thick disks. In two of the galaxies, half of the thick disk mass was from accreted material. In the majority of galaxies in the simulation, the thick disks were found to be older, more metal poor and more enhanced in alpha-elements with respect to iron, indicating that the in situ stars were formed at earlier epochs in the thick disk compared to the thin disk.

Other studies have concentrated on the detailed formation mechanisms of the "in situ" component. Yu et al (2021) emphasized the role of early bursts of star formation in driving thick disk formation in Milky Way type galaxies in the FIRE-2 cosmological simulations. Most recently Chandra et al (2024) put forward a three-phase evolutionary scenario

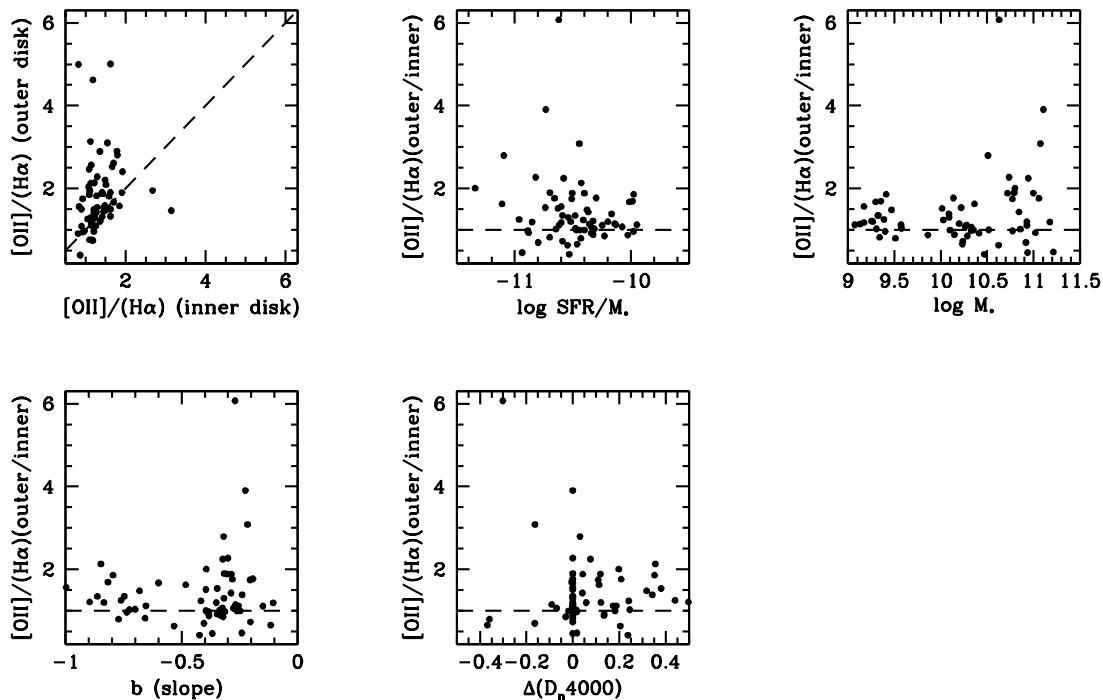


Figure 13. $[\text{OII}]/\text{H}\alpha$ in the outer disk is plotted as a function of $[\text{OII}]/\text{H}\alpha$ in the inner disk. The dashed line indicates the one-to-one linear relation. The next two panels show the ratio of outer disk to inner disk $[\text{OII}]/\text{H}\alpha$ values as a function of the stellar mass and the specific star formation rate of the galaxy. The bottom panels show the ratio of outer disk to inner disk $[\text{OII}]/\text{H}\alpha$ values as a function of the outer disk slope b) and as a function of 4000Å break gradient.

for our own Milky Way: the disordered and chaotic proto-galaxy that forms the bulge, followed by a kinematically hot old disk, and finally a cool-down phase that forms the kinematically cold young disk.

Our work confirms the standard picture for Milky Way type galaxies of a thick disk component that is older than the thin disk. None of the structural or stellar population properties of the thick disk are found to correlate with the present day star formation activity in the thin disk, indicating that the bulk of the thick disk formed at earlier epochs. There is also substantial scatter in the relation between the slope and break radius of the thick disk and the stellar mass of the galaxy over the range $10 < \log M_* < 11$. This is likely indicative of significant variation in satellite accretion histories between different objects, also in line with simulation predictions. Interestingly, our results also echo the diversity found in stellar halo properties of galaxies in the same stellar mass range (Harmsen et al. 2017, Monachesi et al. 2019, Gillhuly et al. 2022).

Our results demonstrate that the structural properties of lower mass disk galaxies differ substantially from those of Milky Way mass galaxies. The lower the mass of the galaxy, the steeper the surface density profile of its thick disk, indicating a smaller contribution to the total disk stellar mass. Since it has been demonstrated that the probability of a bursty star formation history is *higher* for low mass galaxies (see for example Kauffmann 2014), this calls into question the hypothesis that starbursts are responsible for thick disk formation in low mass systems. On the other hand, the

number of merger/accretion events is smaller for low mass galaxies, so the observed trends may be mainly driven by increasing quiescent accretion histories. High resolution simulations of low mass galaxies will be a valuable tool in testing whether the low mass galaxy scaling relations are easily explainable.

Finally, we note that it is important to understand whether the breaks in the $D_n(4000)$ profiles are a fossil record of past merging events. Once again, N-body+hydrodynamical simulation studies with mock IFU cubes smoothed to the same resolution as the MaNGA cubes would be a valuable way to try and understand the origin of such breaks. Such studies would also allow us to assess whether the next generation of deep imaging surveys with the EUCLID telescope in space and the Vera C. Rubin Observatory on the ground would be able to localize the source of the $D_n(4000)$ discontinuities, delineate the morphology of the regions where stellar population properties change abruptly, and help us understand the detailed accretion history of galaxies and their halos in more detail.

Acknowledgements

G.K. thanks Claude-André Faucher-Giguère and Jing Wang for useful discussions. A.M. gratefully acknowledges support by the ANID BASAL project FB210003, by the FONDECYT Regular grant 1212046, and funding from the Max Planck Society through a "PartnerGroup" grant. Funding for SDSS-IV has been provided by the Alfred P.

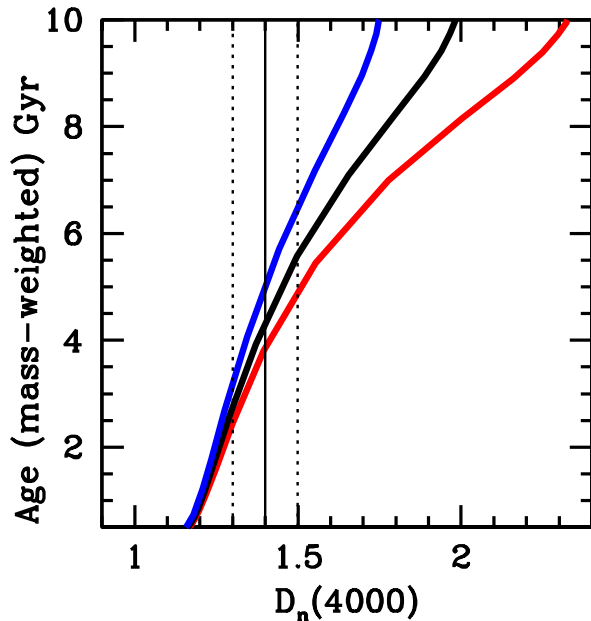


Figure 14. Tracks in the plane of stellar mass-weighted age versus $D_n(4000)$. The blue, black and red curves are for models with 0.25 solar, half solar and solar metallicity. The typical inner disk 4000 Å break strength of 1.4 is marked as a solid line. The typical change in $D_n(4000)$ over a break region of 0.1 is marked as dotted lines on the plot.

Sloan Foundation and Participating Institutions. Additional funding towards SDSS-IV has been provided by the US Department of Energy Office of Science. SDSS-IV acknowledges support and resources from the Centre for High-Performance Computing at the University of Utah. The SDSS web site is www.sdss.org. SDSS-IV is managed by the Astrophysical Research Consortium for the Participating Institutions of the SDSS Collaboration including the Brazilian Participation Group, the Carnegie Institution for Science, Carnegie Mellon University, the Chilean Participation Group, the French Participation Group, Harvard-Smithsonian Center for Astrophysics, Instituto de Astrofísica de Canarias, The Johns Hopkins University, Kavli Institute for the Physics and Mathematics of the Universe (IPMU)/University of Tokyo, Lawrence Berkeley National Laboratory, Leibniz Institut für Astrophysik Potsdam (AIP), Max-Planck-Institut für Astronomie (MPIA Heidelberg), Max-Planck-Institut für Astrophysik (MPA Garching), Max-Planck-Institut für Extraterrestrische Physik (MPE), National Astronomical Observatory of China, New Mexico State University, New York University, University of Notre Dame, Observatorio Nacional/MCTI, the Ohio State University, Pennsylvania State University, Shanghai Astronomical Observatory, United Kingdom Participation Group, Universidad Nacional Autónoma de México, University of Arizona, University of Colorado Boulder, University of Oxford, University of Portsmouth, University of Utah, University of Virginia, University of Washington, University of Wisconsin, Vanderbilt University and Yale University.

Data Availability

Data from this paper will be made available on reasonable request to the corresponding author.

REFERENCES

- Abadi M. G., Benítez-Llambay A., Ferrero I., 2013, *BAAA*, 56, 33
- Abdurro’uf, Accetta K., Aerts C., Silva Aguirre V., Ahumada R., Ajgaonkar N., Filiz Ak N., et al., 2022, *ApJS*, 259, 35. doi:10.3847/1538-4365/ac4414
- Aguado D. S., Ahumada R., Almeida A., Anderson S. F., Andrews B. H., Anguiano B., Aquino Ortíz E., et al., 2019, *ApJS*, 240, 23. doi:10.3847/1538-4365/aaf651
- Bekki K., Chiba M., 2001, *ApJ*, 558, 666. doi:10.1086/322300
- Beom M., Bizyaev D., Walterbos R. A. M., Chen Y., 2022, *MNRAS*, 516, 3175. doi:10.1093/mnras/stac1499
- Blanton M. R., Bershady M. A., Abolfathi B., Albareti F. D., Allende Prieto C., Almeida A., Alonso-García J., et al., 2017, *AJ*, 154, 28. doi:10.3847/1538-3881/aa7567
- Brook C. B., Kawata D., Gibson B. K., Freeman K. C., 2004, *ApJ*, 612, 894. doi:10.1086/422709
- Brook C. B., Stinson G. S., Gibson B. K., Kawata D., House E. L., Miranda M. S., Macciò A. V., et al., 2012, *MNRAS*, 426, 690. doi:10.1111/j.1365-2966.2012.21738.x
- Bruzual G., Charlot S., 2003, *MNRAS*, 344, 1000. doi:10.1046/j.1365-8711.2003.06897.x
- Bundy K., Bershady M. A., Law D. R., Yan R., Drory N., MacDonald N., Wake D. A., et al., 2015, *ApJ*, 798, 7. doi:10.1088/0004-637X/798/1/7
- Chandra V., Semenov V. A., Rix H.-W., Conroy C., Bonaca A., Naidu R. P., Andrae R., et al., 2024, *ApJ*, 972, 112. doi:10.3847/1538-4357/ad5b60
- Comerón S., Elmegreen B. G., Knapen J. H., Salo H., Laurikainen E., Laine J., Athanassoula E., et al., 2011, *ApJ*, 741, 28. doi:10.1088/0004-637X/741/1/28
- Comerón S., Elmegreen B. G., Salo H., Laurikainen E., Holwerda B. W., Knapen J. H., 2014, *A&A*, 571, A58. doi:10.1051/0004-6361/201424412
- Dalcanton J. J., Bernstein R. A., 2000, *AJ*, 120, 203. doi:10.1086/301425
- Drory N., MacDonald N., Bershady M. A., Bundy K., Gunn J., Law D. R., Smith M., et al., 2015, *AJ*, 149, 77. doi:10.1088/0004-6256/149/2/77
- Elias L. M., Sales L. V., Creasey P., Cooper M. C., Bullock J. S., Rich R. M., Hernquist L., 2018, *MNRAS*, 479, 4004. doi:10.1093/mnras/sty1718
- Freeman K. C., 1974, *IAUS*, 58, 129
- Gilhuly C., Merritt A., Abraham R., Danieli S., Lokhorst D., Liu Q., van Dokkum P., et al., 2022, *ApJ*, 932, 44. doi:10.3847/1538-4357/ac6750
- Gilmore G., Reid N., 1983, *MNRAS*, 202, 1025. doi:10.1093/mnras/202.4.1025
- Gunn J. E., 1982, *ac...proc*, 133
- Gunn J. E., Siegmund W. A., Mannery E. J., Owen R. E., Hull C. L., Leger R. F., Carey L. N., et al., 2006, *AJ*, 131, 2332. doi:10.1086/500975
- Harmsen B., Monachesi A., Bell E. F., de Jong R. S., Bailin J., Radburn-Smith D. J., Holwerda B. W., 2017, *MNRAS*, 466, 1491. doi:10.1093/mnras/stw2992

- Ho I.-T., Medling A. M., Bland-Hawthorn J., Groves B., Kewley L. J., Kobayashi C., Dopita M. A., et al., 2016, *MNRAS*, 457, 1257. doi:10.1093/mnras/stw017
- Jones A., Kauffmann G., D'Souza R., Bizyaev D., Law D., Haffner L., Bahé Y., et al., 2017, *A&A*, 599, A141. doi:10.1051/0004-6361/20162980
- Karachentsev I. D., Karachentseva V. E., Parnovskij S. L., 1993, *AN*, 314, 97. doi:10.1002/asna.2113140302
- Kauffmann G., Heckman T. M., White S. D. M., Charlot S., Tremonti C., Peng E. W., Seibert M., et al., 2003, *MNRAS*, 341, 54. doi:10.1046/j.1365-8711.2003.06292.x
- Kauffmann G., 2014, *MNRAS*, 441, 2717. doi:10.1093/mnras/stu752
- Kroupa P., 2001, *MNRAS*, 322, 231. doi:10.1046/j.1365-8711.2001.04022.x
- Lacerda E. A. D., Sánchez S. F., Mejía-Narváez A., Camps-Fariña A., Espinosa-Ponce C., Barrera-Ballesteros J. K., Ibarra-Medel H., et al., 2022, *NewA*, 97, 101895. doi:10.1016/j.newast.2022.101895
- Law D. R., Yan R., Bershady M. A., Bundy K., Cherinka B., Drory N., MacDonald N., et al., 2015, *AJ*, 150, 19. doi:10.1088/0004-6256/150/1/19
- Lehnert M. D., Heckman T. M., 1996, *ApJ*, 462, 651. doi:10.1086/177180
- Merritt A., van Dokkum P., Abraham R., Zhang J., 2016, *ApJ*, 830, 62. doi:10.3847/0004-637X/830/2/62
- Monachesi A., Gómez F. A., Grand R. J. J., Simpson C. M., Kauffmann G., Bustamante S., Marinacci F., et al., 2019, *MNRAS*, 485, 2589. doi:10.1093/mnras/stz538
- Pinna F., Walo-Martín D., Grand R. J. J., Martig M., Fragkoudi F., Gómez F. A., Marinacci F., et al., 2024, *A&A*, 683, A236. doi:10.1051/0004-6361/202347388
- Pohlen M., Balcells M., Lütticke R., Dettmar R.-J., 2004, *A&A*, 422, 465. doi:10.1051/0004-6361:20035932
- Quinn P. J., Hernquist L., Fullagar D. P., 1993, *ApJ*, 403, 74. doi:10.1086/172184
- Read J. I., Lake G., Agertz O., Debattista V. P., 2008, *MNRAS*, 389, 1041. doi:10.1111/j.1365-2966.2008.13643.x
- Sánchez S. F., Barrera-Ballesteros J. K., Lacerda E., Mejía-Narvaez A., Camps-Fariña A., Bruzual G., Espinosa-Ponce C., et al., 2022, *ApJS*, 262, 36. doi:10.3847/1538-4365/ac7b8f
- Sanderson R. E., Garrison-Kimmel S., Wetzel A., Keung Chan T., Hopkins P. F., Kereš D., Escala I., et al., 2018, *ApJ*, 869, 12. doi:10.3847/1538-4357/aaeb33
- Sattler N., Pinna F., Comerón S., Martig M., Falcón-Barroso J., Martín-Navarro I., Neumayer N., 2024, *arXiv*, arXiv:2410.05761. doi:10.48550/arXiv.2410.05761
- Smee S. A., Gunn J. E., Uomoto A., Roe N., Schlegel D., Rockosi C. M., Carr M. A., et al., 2013, *AJ*, 146, 32. doi:10.1088/0004-6256/146/2/32
- Toth G., Ostriker J. P., 1992, *ApJ*, 389, 5. doi:10.1086/171185
- van der Kruit P. C., 1988, *A&A*, 192, 117
- van der Kruit P. C., Searle L., 1981, *A&A*, 95, 105
- Vazdekis A., Sánchez-Blázquez P., Falcón-Barroso J., Cenarro A. J., Beasley M. A., Cardiel N., Gorgas J., et al., 2010, *MNRAS*, 404, 1639. doi:10.1111/j.1365-2966.2010.16407.x
- Velazquez H., White S. D. M., 1999, *MNRAS*, 304, 254. doi:10.1046/j.1365-8711.1999.02354.x
- Wake D. A., Bundy K., Diamond-Stanic A. M., Yan R., Blanton M. R., Bershady M. A., Sánchez-Gallego J. R., et al., 2017, *AJ*, 154, 86. doi:10.3847/1538-3881/aa7ecc
- Wang L., Kauffmann G., 2008, *MNRAS*, 391, 785. doi:10.1111/j.1365-2966.2008.13907.x
- Wu H., Burstein D., Deng Z., Zhou X., Shang Z., Zheng Z., Chen J., et al., 2002, *AJ*, 123, 1364. doi:10.1086/338849
- Yan R., Bundy K., Law D. R., Bershady M. A., Andrews B., Cherinka B., Diamond-Stanic A. M., et al., 2016, *AJ*, 152, 197. doi:10.3847/0004-6256/152/6/197
- Yoachim P., Dalcanton J. J., 2006, *AJ*, 131, 226. doi:10.1086/497970
- Yu S., Bullock J. S., Klein C., Stern J., Wetzel A., Ma X., Moreno J., et al., 2021, *MNRAS*, 505, 889. doi:10.1093/mnras/stab1339